JOURNAL OF THEORETICAL
AND APPLIED MECHANICS
63, 3, pp. 511–523, Warsaw 2025
https://doi.org/10.15632/jtam-pl/202124

MOMENT-CURVATURE RELATION FOR LASER-ASSISTED BENDING OF THIN INCONEL 718 BEAM

Jacek WIDLASZEWSKI[1*], Marcin NOWAK[2], Zdzisław NOWAK[1], Piotr KURP[3]

[1] *Institute of Fundamental Technological Research, Polish Academy of Sciences, Warsaw, Poland*
[2] *Institute of Structural Analysis, Poznan University of Technology, Poznan, Poland*
[3] *Center for Laser Technology of Metals, Kielce University of Technology, Kielce, Poland*

*corresponding author, *jacek.widlaszewski@ippt.pan.pl*

Moment-curvature relations for the thermo-mechanical bending of slender beams made of Inconel 718 in the factory-annealed state are determined in the study. The experimentally validated finite element method (FEM) model with the Johnson–Cook material model is used. For the considered conditions of thermo-mechanical processing, the final beam curvature can be estimated as a linear function of the curvature due to the elastic pre-stress. In processing 1 mm thick material, using laser power 500 W and feed rate 3.33 mm/s, a safe time distance of at least 5.4 minutes is estimated between the presence of high material temperature and the start of precipitation processes.

Keywords: thermo-mechanics; laser-assisted bending; Inconel 718; Johnson–Cook model; curvature.

1. Introduction

Materials with high-temperature strength may cause difficulties both in cold-shaping and hot-working. The interest in thermally-based forming is a response to the needs and challenges involved in the cost-effective and robust manufacturing of sheet metal based products. Local heating offers attractive characteristics for metal forming. The necessary forming force or pressure may be reduced with the desired temperature distribution and controlled heating rates. The thermally assisted processing offers reduced wear of forming tools and the reduction of the spring-back effect (Neugebauer *et al.*, 2006; Duflou & Aerens, 2006; Ponticelli *et al.*, 2018; Widłaszewski *et al.*, 2019). Heat-assisted bending of plates proved to be a flexible and cost-effective forming method for small batch situations (Wei *et al.*, 2021).

A laser beam is a heat source offering an exceptional opportunity to control heat input to the workpiece precisely both in time and space. Hence, laser-assisted manufacturing processes have gained ever increasing attention in recent years (Min *et al.*, 2023; Bammer, 2024; Liao *et al.*, 2024). They have been successfully introduced into stamping, bending, single-point incremental forming, spinning, stretch forming, roll profiling, deep drawing, wire drawing, hydroforming and other technologies (Kratky, 2007; Lauwers *et al.*, 2014). However, for successful development of new forming methods, the thermo-mechanics of the heat-assisted plastic deformation process should be thoroughly analysed and well understood. In parallel, thermal processing should retain

The publication has been funded by the Polish Ministry of Science and Higher Education under the Excellent Science II programme "Support for scientific conferences".
The content of this article was presented during the 40th Danubia-Adria Symposium on Advances in Experimental Mechanics, Gdańsk, Poland, September 24–27, 2024.

or establish the critical material properties, without adverse effects on its microstructure. A safe process window needs to be determined.

One of the recently studied thermo-mechanical bending methods consists in laser bending (Aher & Navthar, 2024) combined with mechanical preload. Fetene *et al.* (2018) used an artificial neural network in modelling the laser-assisted bending of a cantilever beam loaded with a force on the free end. The training and testing data set was obtained by a finite element method (FEM) model, which was validated by experiments. In research on bending and straightening of steel strips, Dutta *et al.* (2018) successfully applied laser scanning and external force generated with an electromagnet. Guo *et al.* (2020) proposed an analytical model to predict angular deformation due to the laser scanning of an elastically pre-stressed cantilever plate. The applied laser heating parameter values fostered the activation of the so-called buckling mechanism, which involves the thermally induced local buckling of a plate.

The present research concerns the thermo-mechanical behaviour of slender prismatic beams made of Inconel 718 alloy. Material selection was dictated by its wide application in structures and components operating at elevated temperatures, e.g., in the aerospace industry. Inconel 718 is a precipitation-hardenable nickel-based alloy having exceptionally high yield, tensile and creep-rupture properties at temperatures up to 700 °C (homologous temperature 0.63), combined with good oxidation resistance. The alloy is usually provided in the solution-annealed or the precipitation-hardened condition. The relatively slow precipitation hardening response of Inconel 718 permits annealing and welding without spontaneous hardening during heating and cooling, as well as repair welding, even in the aged condition. The outstanding resistance to post-weld cracking indicates the feasibility of laser-assisted forming application in manufacturing components made of the alloy. Fabrication of 3D complex components from Inconel 718 sheet metal is of great importance for the aerospace industry (Qu *et al.*, 2012; Prasad *et al.*, 2015; Hongbo & Gaochao, 2015; Tan *et al.*, 2018).

Numerical modelling using FEM is an effective tool to gain insight into the thermo-mechanic processes and the impact of processing parameters. In order to find moment-curvature relations in the considered problem, it is necessary to determine the beam curvature with high accuracy. Physical measurements of the curvature are prone to considerable errors and are difficult to perform, taking into account the application of a high power laser beam during experiments. Therefore, the present analysis is based on an experimentally validated numerical model.

2. Experiment

Experiments were conducted on beams made of commercial solution-annealed Inconel 718 with an average initial grain size of 17.5 µm. Specimens were laser-cut from a rolled sheet to minimize any introduction of residual stresses during material cutting. The chemical composition of the material is shown in Table 1.

Table 1. Chemical composition of Inconel 718 sheet [wt.%].

Ni	Cr	Mo	Nb	Co	Mn	Si	Fe	Al	Ti
52.9	19.83	3.12	4.83	0.05	0.29	0.14	Balance	0.60	1.04

A rectangular specimen 20 mm wide and 1 mm thick was clamped in a cantilever arrangement on the experimental stand, as shown in Fig. 1a. The thermo-mechanical loading is schematically presented in Fig. 1b.

Before heating by a moving laser beam, the specimen was pre-stressed in the elastic state. Mechanical load was introduced with gravity acting on weights mounted at the free end of the beam and on the mass of the specimen (Fig. 1). The vertical dead load F for the elastic pre-stress was 3.04 N. In the initial configuration, the distance between the force application point and the fixture was 175 mm.

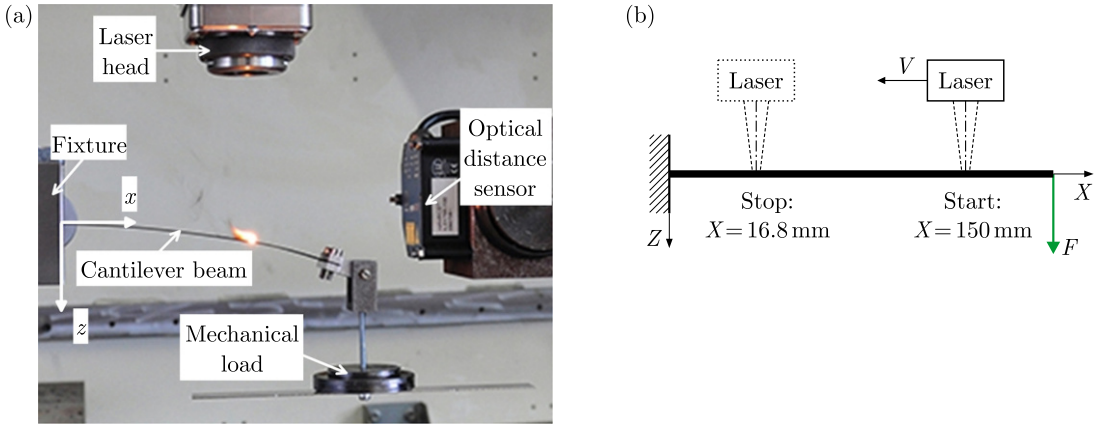

Fig. 1. Experimental setup: (a) a photograph, (b) thermo-mechanical loading scheme.

The pre-stressed beam was subjected to heating with a moving laser beam produced by the TruFlow6000 CO_2 laser which operated in the continuous-wave (CW) mode. A rectangular 20 mm × 2 mm laser spot was formed in the laser head using a facet mirror. The so-called mode shot in Fig. 2 shows a view of a plexiglass plate after short irradiation using the applied laser beam. The picture corresponds with the distribution of radiation power over the laser beam spot.

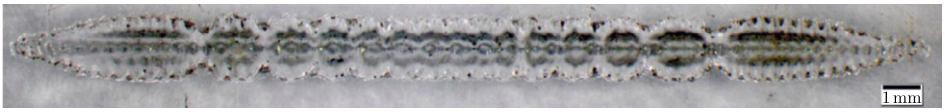

Fig. 2. Plexiglas plate after the mode shot performed with the applied laser beam.

The laser spot covered the whole width of the specimen and moved from the starting position $X = 150$ mm towards the final position $X = 16.8$ mm (Fig. 1b) with constant velocity. This scanning scheme minimized the unwanted influence of the laser beam divergence on laser spot dimensions.

The CO_2 laser radiation of the 10.6 μm wavelength incident at the right angle of the material surface is very poorly absorbed by perfectly clean, flat and smooth metal surfaces. The value of the radiation absorption coefficient rarely exceeds 0.1 for metals in such conditions.

An increase in absorptivity is observed with the increase in surface roughness and temperature. An improvement of energy transfer may be achieved by covering the processed material with an absorptive layer. Such a role can be played by oxides of the metal and various additional materials covering the surface in the form of powder or paint, e.g., graphite powder or a paint containing oxide pigments. Insulators generally have good absorptivity at long radiation wavelengths. Hence, coatings used in processing metallic materials with the CO_2 laser beam often contain dielectrics. A flat black paint is an excellent absorber but a flat white paint is also a highly effective absorber for the infrared radiation, despite its visual appearance.

Surface films may act as an anti-reflection coating due to the interference coupling. The destructive interference of the reflected ray occurs for the film thickness matched with the radiation wavelength. For the destructive interference of the CO_2 laser radiation, the film thickness value should be around 7.95 μm, 13.25 μm, 18.55 μm, and so on in the arithmetic progression.

The coating thickness should not be too large, as in the extreme conditions it can form a thermal barrier considerably affecting the heat flow to the underlying material. However, exothermic metal/oxide coatings may intensify heat input to the processed material. Too thin a coating may undergo a quick degradation without any noticeable effect on the radiation energy transfer. During laser irradiation the absorptive layer should be present at least till the rising temperature of the material surface starts playing a significant role in material absorptivity. Graphite spraying is used both to initially improve energy coupling and to prevent the excessive

material surface temperature rise, the so-called thermal runaway, which impairs the thermal stability of processing. In order to achieve an effective laser treatment with high repeatability, it is necessary to ensure uniform and reproducible application of the absorptive coating to the workpiece surface.

The polished Inconel 718 subject to the CO_2 laser radiation in the air environment has absorptivity between 0.2 and 0.22 in the temperature range 227 °C–1227 °C. Specimens used in this study were covered with an absorptive layer of a black paint in order to improve and stabilize the transfer of laser beam energy into the material. The surface coating thickness was measured with a Mitutoyo Surftest SJ-301 device in a series of preliminary tests with X5CrNi18-10 stainless steel specimens (Kurp *et al.*, 2016). The average thickness of the coating was 8.13 µm with a standard deviation of 0.64 µm.

In order to determine the radiation absorption coefficient, the specimen surface temperature was measured using the OPTRIS CTL G5H CF2 pyrometer. The device operates at a 5.2 µm radiation wavelength and therefore is insensitive to the CO_2 laser radiation reflected from the specimen surface.

The free-end deflection of the specimen during thermo-mechanical loading and unloading processes was measured by a non-contact method. The optical displacement sensor MicroEpsilon LLT1700 measured the vertical displacement component of an auxiliary flat metal plate attached to the holder of weights.

A series of preliminary experiments was performed using laser beam velocity $v = 3.33$ mm/s and laser power 200 W, 300 W, 350 W, 400 W, 500 W, 550 W, and 650 W. It was found that considerable bending deformation is produced using 500 W laser power. The plastic collapse of the processed beam occurred when applying higher laser power. Hence, laser beam velocity $v = 3.33$ mm/s and the laser power 500 W were applied in the main thermo-mechanical bending experiments.

3. Numerical modelling

Spatial coordinates of material points in the initial (reference) configuration of the body are denoted by (X, Y, Z), while those of actual configuration, i.e., after deformation, are denoted by (x, y, z). The thermo-mechanical bending process was modelled in two sequentially coupled analyses, using the commercial FEM program ABAQUS, Version 2016. The symmetry of the object, load and boundary conditions allowed only a half of the considered beam, $0 \leq Y \leq 10$ mm, to be modelled, as shown in Fig. 3a. A regular mesh with hexahedral finite elements of dimensions 0.2 mm× 0.5 mm× 0.1 mm (in directions X, Y, and Z, respectively) was used.

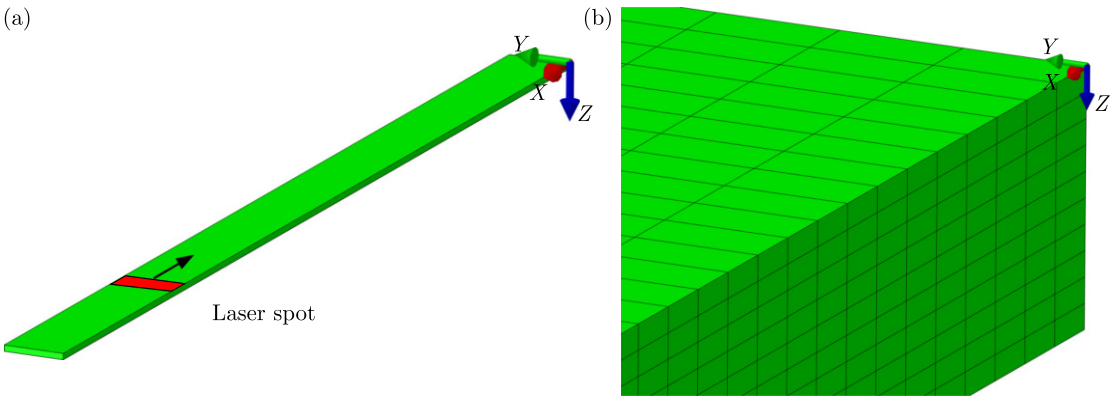

Fig. 3. Numerical model domain: (a) an overall view, (b) a detailed view of the finite element mesh.

The heat transfer analysis was performed in the initial configuration. The top-hat radiation energy distribution over the rectangular laser spot was assumed. A dedicated user subroutine DFLUX modelled the moving laser beam, treated as a surface heat source. The calculated

temperature field and mechanical pre-stressing were subsequently used as thermo-mechanical loading in a quasi-static analysis.

Linear DC3D8 elements for the thermal problem and compatible C3D8 elements for the mechanical problem were applied. As the modelled laser spot had a dimension of 2 mm in the X-direction, the heat input from the moving laser beam was distributed over 10 rows of finite elements in the direction of laser scanning. Ten layers of elements were used in the material thickness direction (axis Z). Such a design of the finite element mesh enabled accurate, numerically-effective modelling of the temperature field and finally the bending effect due to the temperature gradient and mechanical pre-stressing. The regular mesh is also convenient for post-processing of simulation results.

The mesh consisted of 141600 elements and 163779 nodes. No strict mesh convergence study was performed, as numerical results were verified with experimental data. The complete computation time for both the thermal and mechanical analyses was 4 hours using 8-core processor operating at 3.6 GHz frequency.

The temperature dependence of material data was respected in simulations (Nowak *et al.*, 2019). A particular role in thermo-mechanical modelling is played by the application of a suitable material constitutive model with an accurate strain rate and temperature dependency of the yield stress σ_Y^T. The Johnson–Cook (JC) material model was applied in the study:

$$\sigma_Y^T\left(\varepsilon^{pl},\dot{\varepsilon}^{pl},T\right)=\left[A_{\mathrm{JC}}+B\cdot\left(\varepsilon^{pl}\right)^n\right]\left[1+C_{\mathrm{JC}}\cdot\ln\left(\frac{\dot{\varepsilon}^{pl}}{\dot{\varepsilon}_0}\right)\right][1-(T^*)^m], \tag{3.1}$$

where ε^{pl} is the plastic strain component, $\dot{\varepsilon}_0$ ($0.001\,\mathrm{s}^{-1}$ in this work) is the reference strain rate, $T^*=(T-T_r)/(T_m-T_r)$, T_m is the melting temperature (1250 °C in this work) and the transition temperature T_r is assumed 20 °C in this work, A_{JC} is the yield stress under the transition temperature and the reference strain rate, B and n are strain hardening coefficient and exponent, respectively, C_{JC} describes strain rate hardening, and m stands for thermal softening effects.

The values of JC parameters are listed in Table 2 (Nowak *et al.*, 2019), while the assumed stress-strain-temperature behaviour for Inconel 718 is presented in Fig. 4.

Table 2. Parameters of the Johnson–Cook model.

A_{JC} [MPa]	B [MPa]	C_{JC}	m	n
450	2100.95	0.02	1.5	0.76

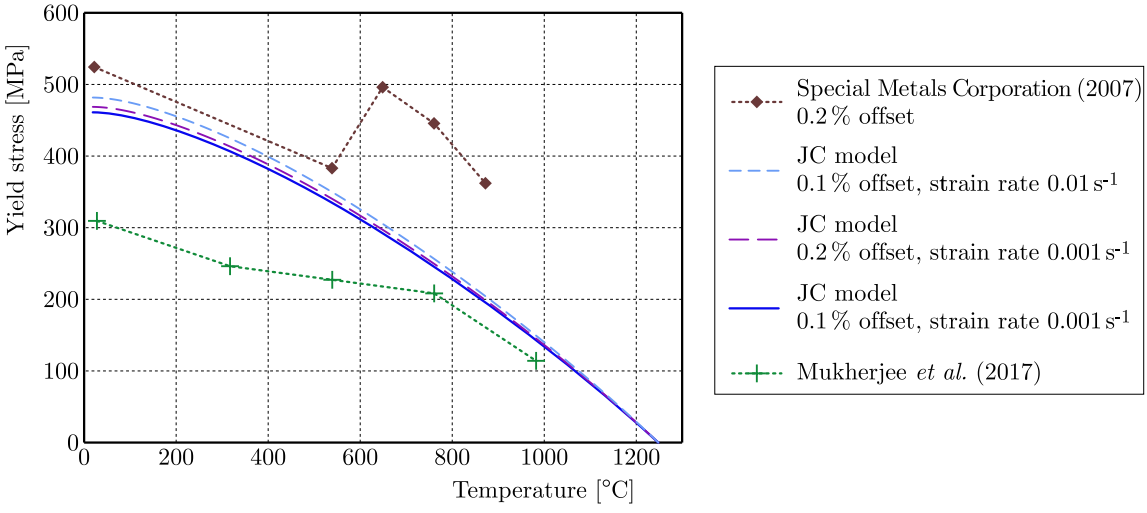

Fig. 4. Yield stress dependence of the annealed Inconel 718 on temperature.

The developed numerical model was used to simulate the thermo-mechanical behaviour of the Inconel 718 beam both with elastic pre-stress and without it. To account for large displacements, the geometric nonlinearity was respected in simulations and the parametric configuration representation was used in the post-processing of simulation results.

Experimental validation of the applied numerical model is crucial for the analysis value. The radiation absorption coefficient A and heat dissipation parameters were calibrated in a number of numerical simulations by comparing their results with the surface temperature measured in the experiment. A good agreement of results was obtained for $A = 0.37$, convection coefficient $5\,\mathrm{W/(m \cdot K)}$ and emissivity value 0.75 (Fig. 5). Strong oscillations visible in the temperature signal recorded during the experiment result from burning of the absorptive layer, as seen in the photograph in Fig. 1a.

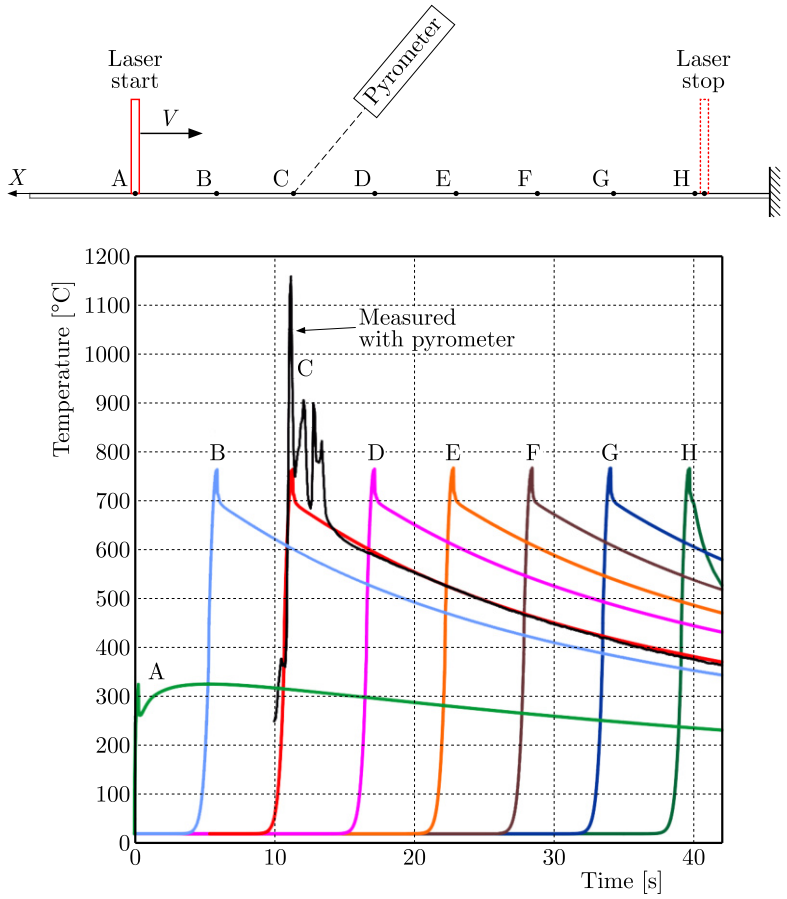

Fig. 5. Temperature variation at selected locations of the upper surface ($Y = 0$, $Z = 0$).

Experimental measurements and simulation results regarding the free-end deflection during laser scanning of the elastically pre-stressed beam are found to match well (Fig. 6). The reasonably close agreement of the temperature and deflection calculated in the simulations with experimental data is considered the numerical model validation.

4. Results

4.1. Temperature distribution and beam configuration

Figures 7 and 8 show the changes in surface temperature distribution and beam configuration for selected positions of the laser beam during scanning. Beam shapes (Fig. 8) present total deformation, i.e., due to the mechanical and thermal load, while the free-end deflection in Fig. 6 was measured starting from the mechanical pre-stressing configuration.

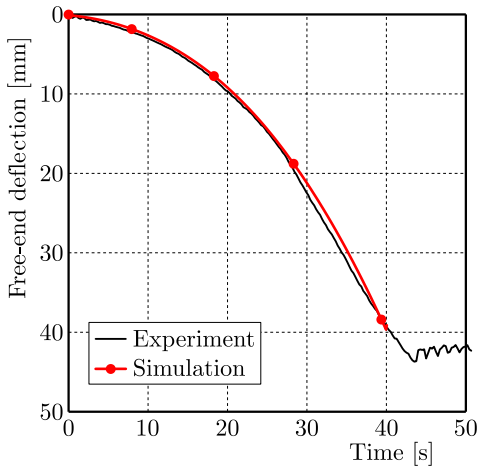

Fig. 6. Free-end deflection of the beam during thermo-mechanical bending.

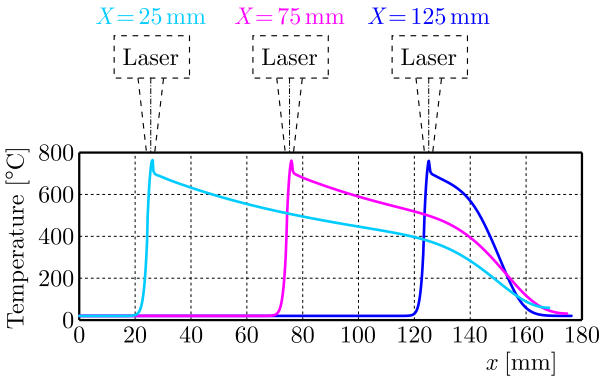

Fig. 7. Surface temperature distribution for laser beam positions $X = 125\,\text{mm}$, $75\,\text{mm}$, and $25\,\text{mm}$ ($Y = 0$, $Z = 0$).

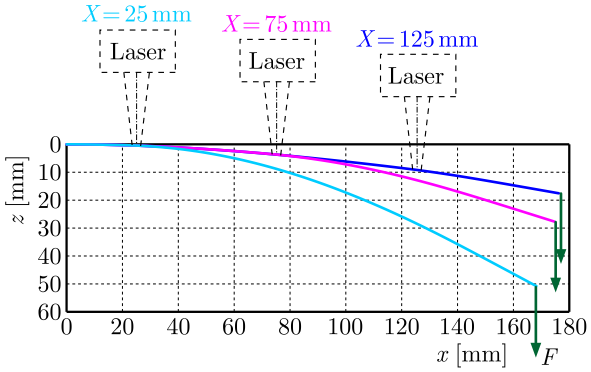

Fig. 8. Beam configurations for laser beam positions $X = 125\,\text{mm}$, $75\,\text{mm}$, and $25\,\text{mm}$ ($Y = 0$, $Z = 0$).

4.2. Thermal cycle

The determined temperature field variation enables the calculation of the thermal cycle which the processed material experiences during laser scanning. Figure 9 presents a typical evolution of temperature at the workpiece surface in relation to the time-temperature-transformation (T-T-T) diagram of Inconel 718. Localized heating with the moving laser beam results in a thermal cycle short enough to avoid the occurrence of unwanted microstructure changes. In the presented example, it offers a process window of over five-minute width, sufficient to induce plastic deformation and to cool down the material safely.

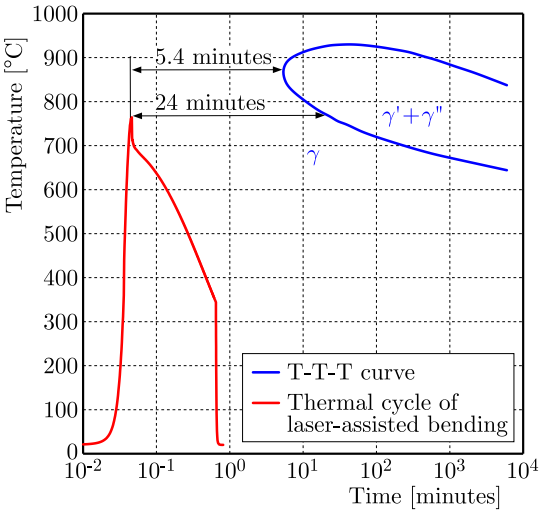

Fig. 9. Surface temperature cycle overlapped on the T-T-T diagram for Inconel 718 alloy (γ – metal matrix, γ' and γ'' – strengthening phases).

4.3. Curvature calculation

Determination of the moment-curvature relations in the considered problem requires the application of a curvature calculation method, which is capable of providing the necessary accuracy of results. Identification of the involved deformation mechanisms requires a careful separation of the contributing factors. Poor accuracy or excessive numerical noise of the calculated curvature values can make it impossible to draw meaningful conclusions from the moment-curvature relations in thermo-mechanical processing.

Two methods were applied to calculate beam curvature distributions after consecutive steps of the considered thermo-mechanical bending process. The first method is based on a discrete description of the beam axis as a 2-D curve. The second one uses the strain field linearization concept and strain values on the material boundary. While the first method involves numerical differentiation over some segment of the curve, the second method is based on the strain distribution over the considered cross-section of the material, and thus is more suitable to reveal local features of the curvature distribution.

4.3.1. Differential geometry approach

The beam axis ($Y = 0$, $Z = h/2$) is treated as a plane curve in the discrete parametric description $x = x(p)$, $z = z(p)$, where x, z are nodal coordinates, p is the parameter of the curve. The X-coordinate of a node in the initial configuration is used as the curve parameter ($p = X$).

The beam axis curvature C is calculated using the formula

$$C = \frac{|z''x' - x''z'|}{(x'^2 + z'^2)^{3/2}}, \tag{4.1}$$

where operators $()'$ and $()''$ denote the first and the second derivative with respect to the parameter p, respectively (Toponogov, 2006). For simplicity, the curvature and bending moment values are presented with the positive sign in this paper.

The finite difference method is used to calculate derivatives x' and z'. The symmetric difference quotient formula is applied for the first derivative:

$$f'(p) \approx \frac{f(p + \Delta p) - f(p - \Delta p)}{2\Delta p}, \tag{4.2}$$

where Δp is the numerical differentiation parameter of a possibly small value.

Similarly, the central difference approximation was used for the second derivatives x'' and z''

$$f''(p) \approx \frac{f(p+\Delta p) - 2f(p) + f(p-\Delta p)}{\Delta p^2}. \tag{4.3}$$

Numerical differentiation using a small value of parameter Δp is sensitive to errors resulting from the limited representation precision of numerical data, i.e., round-off errors. Low round-off and truncation errors were achieved using $\Delta p = 3\,\text{mm}$, with $x(p)$, $z(p)$, and p expressed in millimetres.

4.3.2. Strain linearization approach

In general, the longitudinal strain across a section of the considered beam may be decomposed into the following components: (1) average membrane, (2) linear bending, and (3) peak strain. Figure 10 presents an example of the variation in the longitudinal strain component over the material thickness $\varepsilon_{xx}(Z)$ ($X = 100$, $Y = 0$) after the consecutive steps of the process: (1) mechanical pre-stress, (2) laser heating, and (3) after cooling and removing of the mechanical load, i.e., in the final state. Dashed lines in the figure indicate linear approximations of the strain distribution. It is visible that the longitudinal strain component ε_{xx} may be fairly accurately treated as linear with respect to the coordinate Z. This conclusion justifies decomposing the through-thickness strain state into membrane and bending components.

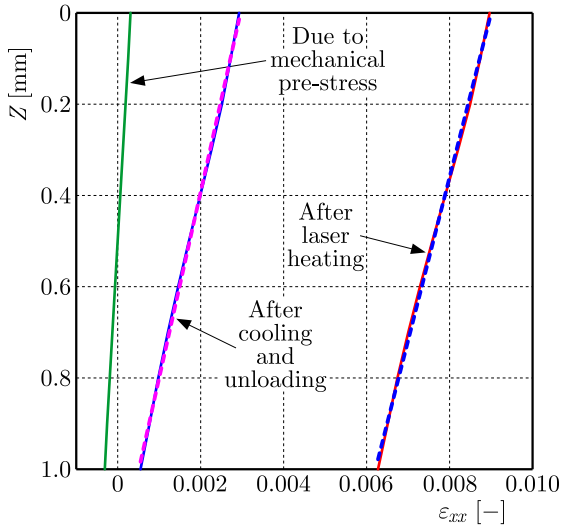

Fig. 10. Longitudinal strain distribution over material thickness ($X = 100$, $Y = 0$).

The example of strain distribution over material thickness (Fig. 10) reveals that the considered thermo-mechanical processing may result in thermo-plastic stretching of material fibers over the whole thickness of the processed workpiece. In this case, the notion of the neutral axis can be related only to a theoretical line located out of the deformed material. It can no longer be identified with a real material fiber. Such a considerable "shift" of the neutral axis has to be respected in calculating the beam curvature based on the strain field.

By denoting longitudinal strain at the extreme points of a cross-section as ε_{IN} and ε_{OUT}, for the inner and outer material fibers of the deformed beam, respectively, one can easily derive strain components of the decomposition and the curvature as

$$\varepsilon_b = \frac{\varepsilon_{\text{OUT}} - \varepsilon_{\text{IN}}}{2}, \quad \varepsilon_m = \frac{\varepsilon_{\text{OUT}} + \varepsilon_{\text{IN}}}{2}, \quad \frac{1}{R_0} = \frac{\varepsilon_{\text{OUT}} - \varepsilon_{\text{IN}}}{h}, \quad \frac{1}{R} = \frac{1}{1+\varepsilon_m}\frac{1}{R_0}, \tag{4.4}$$

where ε_b, ε_m are the bending and membrane strain components, respectively, $1/R_0$ is the curvature of the middle beam layer ($Z = h/2$) for the case with no shift of the neutral axis ($\varepsilon_{\text{OUT}} = -\varepsilon_{\text{IN}}$), $1/R$ is the actual curvature when the neutral axis shift is present.

A comparison of the curvature calculated using both approaches is shown in Fig. 11. The strain linearization approach is more sensitive to such a local phenomenon as transient deformation due to temperature gradient over material thickness in the laser spot vicinity (see Fig. 11, vicinity of the laser track end at $X = 16.8\,\text{mm}$). The curvature distribution obtained using the differential geometry approach has much smaller numerical noise, although it involves numerical differentiation. In general, the results of both calculation methods agree well with each other. On the basis of such verification, curvature calculated using the differential geometry approach is used in further analysis.

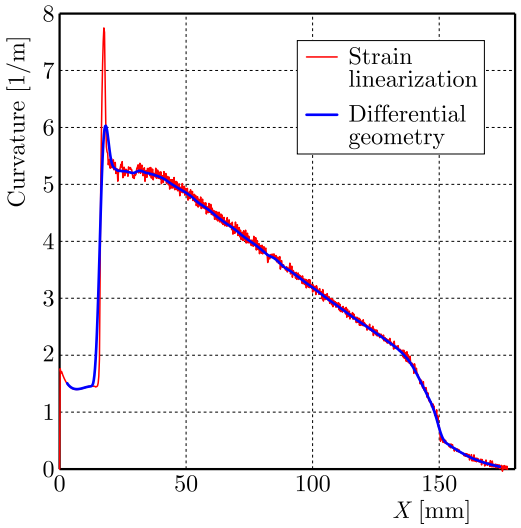

Fig. 11. Beam axis curvature immediately after the step of laser scanning ($Y = 0$, $Z = h/2$).

4.4. Curvature changes in thermo-mechanical processing

Figure 12 presents the following beam curvature characteristics: (1) after mechanical prestressing (marked as "elastic"), (2) after laser scanning followed by cooling the beam to the initial temperature (marked as "thermo-elastic-plastic"), and (3) after final unloading (marked as "plastic (final)"), calculated using the differential geometry approach. Three regions of thermo-elastic-plastic and plastic curvature characteristics can be distinguished. In the central region, from $X = 50$ to $X = 130$, the curvature practically depends linearly on the coordinate X. The other two regions, $X < 50$ and $X > 130$, include the start and stop positions of laser

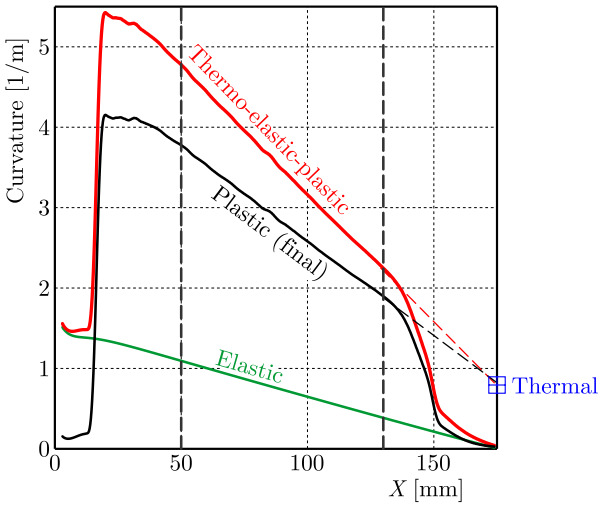

Fig. 12. Beam axis curvature distribution after specific processing steps.

scanning (cf. Figs. 1b and 5). Hence, the changes in thermal conditions greatly affect curvature characteristics in these regions.

Even without mechanical pre-stress ($F = 0$), the beam undergoes considerable plastic deformation, solely due to the load from a moving heat source. The related curvature is 0.797 (1/m) and in Figs. 12 and 13 is marked as "thermal". The so-called convex deformation occurred, such as when the heated material surface assumes the convex shape (Widłaszewski, 2022).

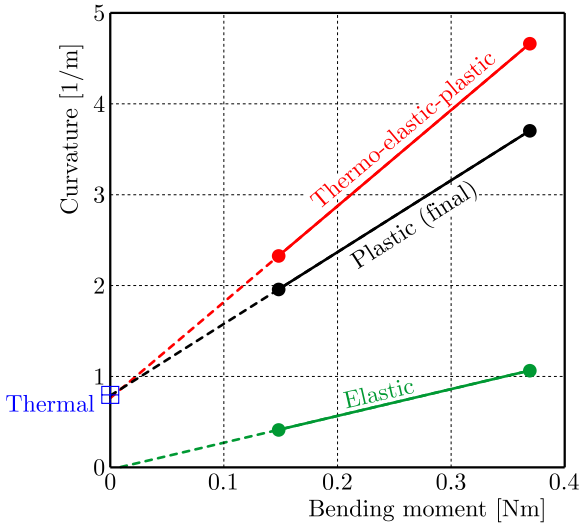

Fig. 13. Moment-curvature relations for specific steps of thermo-mechanical bending.

For the step of mechanical elastic pre-stressing, the calculated curvature agrees well with the analytical solution of the classical Euler-Bernoulli beam theory. Moment-curvature dependences shown in Fig. 13 were calculated for the central region of the beam, for $X = 50$ to $X = 130$. Curvature characteristics calculated after thermo-mechanical processing and after final unloading can be extrapolated up to the bending moment value 0, which corresponds to the pure thermal load case. The results of both extrapolations agree well with the curvature value determined in the simulation without pre-stress ($F = 0$).

Relations between the calculated curvatures can be characterized by the following dimensionless coefficients:

$$k_{\mathrm{TEP}} = \frac{(C_{\mathrm{TEP}} - C_T)}{C_E}, \qquad k_U = \frac{(C_{\mathrm{TEP}} - C_U)}{C_E}, \tag{4.5}$$

where C_T is the curvature due to purely thermal loading, C_E is the curvature after elastic pre-stressing, C_{TEP} is the curvature after thermo-elastic-plastic processing and cooling, still under mechanical load, C_U is the final curvature, i.e., after the final unloading.

The coefficient k_{TEP} represents the relation of the curvature change $(C_{\mathrm{TEP}} - C_T)$ resulting from thermo-mechanical processing to the curvature due to the initial elastic pre-stressing (C_E). The second coefficient, k_U, shows how the curvature change due to the final unloading $(C_{\mathrm{TEP}} - C_U)$ relates to the curvature after the initial elastic loading (C_E). Within the region $50 < X < 110$, the value of the coefficient k_{TEP} varies by less than 0.7 % of the mean value 3.64, while the value of the coefficient k_U changes by less than 1.3 % of the mean value 0.903. Hence, one can conclude that the curvature resulting from the considered thermo-mechanical processing can be estimated as a linear function of the curvature due to the elastic pre-stress:

$$C_{\mathrm{TEP}} = k_{\mathrm{TEP}} C_E + C_T, \qquad C_U = C_{\mathrm{TEP}} - k_U C_E. \tag{4.6}$$

The curvature change due to removal of the mechanical load describes the elastic response opposite to the deformation produced during pre-stressing. However, it concerns the beam with

the residual stress field after considerable plastic deformation. Hence, the value of the coefficient k_U is not exactly 1.

5. Conclusions

Phenomenological moment-curvature relations for the laser-assisted bending of a slender Inconel 718 beam were formulated using the experimentally validated FEM model. For the analysed body and its thermal and mechanical loading conditions, the curvature after the laser-induced plastic deformation process can be estimated as a linear function of the curvature produced due to the elastic pre-stressing. The analysis revealed the presence of pure thermally induced deformation in the final change of the curvature. In processing 1 mm thick material, using laser power 500 W and feed rate 3.33 mm/s, a safe time distance of at least 5.4 minutes is estimated between the presence of high material temperature and the start of the precipitation processes. For the effective laser-assisted bending, the external mechanical load should be applied consistently with the deformation effect of the heat source alone, which under the considered conditions was the convex bending. The determined moment-curvature relations can be used in the design and optimization of thermo-mechanical processing.

Acknowledgments

The research reported herein was partly supported by a grant from the National Centre for Research and Development (no. PBS/A5/47/2015).

References

1. Aher, V., & Navthar, R.R. (2024). A comprehensive review on laser bending of advanced materials. *Lasers in Manufacturing and Materials Processing*, *11*(3), 814–852. https://doi.org/10.1007/s40516-024-00261-w

2. Bammer, F. (2024). Optimized heat distributions for laser-assisted forming. *Journal of Engineering*, *2024*(1), Article 9470839. https://doi.org/10.1155/2024/9470839

3. Duflou, J.R., & Aerens, R. (2006). Force reduction in bending of thick steel plates by localized preheating. *CIRP Annals*, *55*(1), 237–240. https://doi.org/10.1016/S0007-8506(07)60406-5

4. Dutta, P.P., Kalita, K., & Dixit, U.S. (2018). Electromagnetic-force-assisted bending and straightening of AH36 steel strip by laser irradiation. *Lasers in Manufacturing and Materials Processing*, *5*(3), 201–221. https://doi.org/10.1007/s40516-018-0062-6

5. Fetene, B.N., Shufen, R., & Dixit, U.S. (2018). FEM-based neural network modeling of laser-assisted bending. *Neural Computing & Applications*, *29*(6), 69–82. https://doi.org/10.1007/s00521-016-2544-9

6. Guo, Y., Shi, Y., Wang, X., Sun, R., & Bing, Z. (2020). An analytical model of laser bending angle under preload. *The International Journal of Advanced Manufacturing Technology*, *108*(7–8), 2569–2577. https://doi.org/10.1007/s00170-020-05521-5

7. Hongbo, D., & Gaochao, W. (2015). Effect of deformation process on superplasticity of Inconel 718 alloy. *Rare Metal Materials and Engineering*, *44*(2), 298–302. https://doi.org/10.1016/S1875-5372(15)30023-0

8. Kratky, A. (2007). Laser assisted forming techniques. *Proceedings Volume 6346, XVI International Symposium on Gas Flow, Chemical Lasers, and High-Power Lasers*, Article 634615. https://doi.org/10.1117/12.738146

9. Kurp, P., Mucha, Z., Mulczyk, K., Gradoń, R., & Trela, P. (2016). The influence of surface preparation on the absorption coefficient of laser radiation. *Proceedings Volume 10159, Laser Technology 2016: Progress and Applications of Lasers*, *10159*, Article 101590M. https://doi.org/10.1117/12.2257992

10. Lauwers, B., Klocke, F., Klink, A., Tekkaya, A.E., Neugebauer, R., & Mcintosh, D. (2014). Hybrid processes in manufacturing. *CIRP Annals*, *63*(2), 561–583. https://doi.org/10.1016/j.cirp.2014.05.003

11. Liao, W.-X., Lee, W.-T., Lin, C.-K., Tung, P.-C., & Ho, J.-R. (2024). Innovative laser-assisted glass bending approaches using a near-infrared continuous wave laser. *Optics and Lasers in Engineering*, *178*, Article 108162. https://doi.org/10.1016/j.optlaseng.2024.108162

12. Min, J., Wang, J., Lian, J., Liu, Y., & Hou, Z. (2023). Laser-assisted robotic roller forming of ultrahigh-strength steel QP1180 with high precision. *Materials*, *16*(3), Article 1026. https://doi.org/10.3390/ma16031026

13. Mukherjee, T., Zhang, W., & DebRoy, T. (2017). An improved prediction of residual stresses and distortion in additive manufacturing. *Computational Materials Science*, *126*, 360–372. https://doi.org/10.1016/j.commatsci.2016.10.003

14. Neugebauer, R., Altan, T., Geiger, M., Kleiner, M., & Sterzing, A. (2006). Sheet metal forming at elevated temperatures. *CIRP Annals*, *55*(2), 793–816. https://doi.org/10.1016/j.cirp.2006.10.008

15. Nowak, Z., Nowak, M., Pecherski, R.B., Wisniewski, K., Widłaszewski, J., & Kurp, P. (2019). Computational modeling of thermoplastic behavior of Inconel 718 in application to laser-assisted bending of thin-walled tubes. *International Journal for Multiscale Computational Engineering*, *17*(3), 317–338. https://doi.org/10.1615/IntJMultCompEng.2019029858

16. Oradei-Basile, A., & Radavich, J.F. (1991). A current T-T-T diagram for wrought alloy 718. In E.A. Loria (Ed.), *Superalloys 718, 625 and various derivatives* (pp. 325–335). The Minerals, Metals & Materials Society. Warrendale. https://doi.org./10.7449/1991/SUPERALLOYS_1991_325_335

17. Ponticelli, G.S., Guarino, S., & Giannini, O. (2018). A fuzzy logic-based model in laser-assisted bending springback control. *The International Journal of Advanced Manufacturing Technology*, *95*(9–12), 3887–3898. https://doi.org/10.1007/s00170-017-1482-8

18. Prasad, K.S., Kamal, T., Panda, S.K., Kar, S., Narayana Murty, S.V.S., & Sharma, S.C. (2015). Finite element validation of forming limit diagram of IN-718 sheet metal. *Materials Today: Proceedings*, *2*(4–5), 2037–2045. https://doi.org/10.1016/j.matpr.2015.07.174

19. Qu, F.S., Lu, Z., Xing, F., & Zhang, K.F. (2012). Study on laser beam welding/superplastic forming technology of multi-sheet cylinder sandwich structure for Inconel718 superalloy with ultra-fine grains. *Materials & Design*, *39*, 151–161. https://doi.org/10.1016/j.matdes.2012.02.002

20. Special Metals Corporation (2007). *Inconel Alloy 718*. Retrieved December 12, 2024, from https://www.specialmetals.com/documents/technical-bulletins/inconel/inconel-alloy-718.pdf

21. Tan, Y.B., Ma, Y.H., & Zhao, F. (2018). Hot deformation behavior and constitutive modeling of fine grained Inconel 718 superalloy. *Journal of Alloys and Compounds*, *741*, 85–96. https://doi.org/10.1016/j.jallcom.2017.12.265

22. Toponogov, V.A. (2006). *Differential geometry of curves and surfaces. A Concise Guide*. Boston: Birkhäuser.

23. Wei, B., Zhang, F., He, K., Zhou, C., & Du, R. (2021). Heat-assisted incremental bending of metal plates with unsymmetrical curvatures. *The International Journal of Advanced Manufacturing Technology*, *114*(11–12), 3437–3448. https://doi.org/10.1007/s00170-021-07067-6

24. Widłaszewski, J., Nowak, M., Nowak, Z., & Kurp, P. (2019). Laser-assisted thermomechanical bending of tube profiles. *Archives of Metallurgy and Materials*, *64*(1), 421–430. https://doi.org/10.24425/amm.2019.126268

25. Widłaszewski, J. (2022). Laser micro bending mechanism for high-precision adjustment in mechatronic systems. In J. Holnicki-Szulc, D. Wagg, & Ł. Jankowski (Eds.), *7th European Conference on Structural Control. Book of abstracts and selected papers* (pp. 262–269). Institute of Fundamental Technological Research and Committee on Mechanics, Polish Academy of Sciences. http://eacs2022.ippt.pan.pl/EACS%202022%20-%20Book.pdf

Manuscript received December 12, 2024; accepted for publication February 20, 2025; published online June 23, 2025.